Geomechanics of hydraulic fracturing microseismicity: Part 2. Stress state determination

Seth Busetti and Ze'ev Reches

ABSTRACT

We investigate the hydraulic fracturing process by analysis of the associated microseismicity. In part 1, we recognized double-couple and hybrid microseismic events and their fault plane orientations. Critical stress (instability) and stress inversion techniques were used to assess fracture activation conditions. In part 2, we apply results from the tensile source model to investigate how activated faults relate to the stress state and geologic setting. We assess potential mechanisms for induced microseismicity including leakoff and diffuse pressurized fracture network flow, stress shadowing adjacent to large parent hydraulic fractures, and crack tip stress perturbations. Data are from the Mississippian Barnett Shale, Texas, and include microseismic events from sequential pumping stages in two adjacent horizontal wells that were recorded in two downhole monitor wells, as well as operations, wellbore-derived stress, and natural fracture data.

Results point to activation of inclined faults whose orientation is dominantly northeast–southwest and vertical north–south faults. The activation stress states for a range of modeling scenarios show stress rotation, decreased mean stress, and increased deviatoric stress. This stress state cannot be explained by sidewall leakoff in the stress shadow region adjacent to hydrofractures, but is consistent with hybrid and shear activation obliquely ahead of pressurized fractures. Information about hydrofracture evolution and operationally related dynamic stress change is obscured by geomechanical heterogeneity that is likely geologic in nature. The most compelling observation is that the most highly misoriented microseismic faults occur in the same vicinity as a carbonate-dominated submarine fan feature that was previously expected to act as a minor fracture barrier.

AUTHORS

SETH BUSETTI ~ ConocoPhillips, 600 N. Dairy Ashford, Houston, Texas 77079; seth.busetti@conocophillips.com

Seth Busetti received a B.S. degree in geological engineering from the Colorado School of Mines and an M.S. degree and Ph.D. in structural geology from the University of Oklahoma. Busetti is currently employed by ConocoPhillips and works in a subsurface technology position focusing on applied structural geology and geomechanics problems worldwide. He is involved in projects involving fracture and fault mechanics, fluid flow in fractured reservoirs, and geomechanics in nonconventional reservoirs.

ZE'EV RECHES ~ ConocoPhillips School of Geology and Geophysics, University of Oklahoma, 100 East Boyd Street Suite 710, Norman, Oklahoma 73019; reches@ou.edu

Ze'ev Reches received B.S. and M.S. degrees in geology from Hebrew University, Israel, and a Ph.D. in structural geology from Stanford University. Reches serves as professor of structural geology at the University of Oklahoma. His prior work includes positions at Arizona State University, Stanford University, and US Geological Survey at Menlo Park, California, and Hebrew University, Israel. Research interests include earthquake and fault processes and rock mechanics.

INTRODUCTION

Microseismic monitoring is a widely used tool to map hydraulic fractures for optimizing borehole position, stimulated rock volume, and production parameters, as well as for real-time monitoring of hydraulic fracture growth. The activation mechanisms of the microseismic events are difficult to determine and still poorly understood. Thus, only a few tools exist for objectively discerning the mechanisms of microseismicity, and analysis of microseismic patterns is commonly based on idealized models of hydraulic fracturing. Hydraulic fracture experiments indicate that nearly all detected acoustic emissions events are in immediate proximity to the large, induced hydraulic fractures (e.g., Byerlee and Lockner, 1977; Ishida et al., 2004; Athavale and Miskimins, 2008; Chitrala et al., 2011). Following this experimental finding for field data, one might ignore sparse or detached microseismic events or events that are inconsistent with the expected linear trend of the hydraulic fracture. Further, fault and fracture interactions in the field and complex reservoir behavior are not represented in the small-scale laboratory setting. Other approaches, which include fractal analysis of microseismicity or magnitude distribution (Vermylen and Zoback, 2011; Grob and van der Baan, 2011; Sil et al., 2012), provide rational hypotheses about the in situ stress regime that are likely to be oversimplified.

Our present objective is to improve the interpretation of the hydraulic fracturing process by determination of fault orientations of microseismic events, calculation of the activating stress, and relating this activation to the hydraulic fracture. We assume that the microseismic events reflect activation of critically stressed natural fractures and faults in the reservoirs, but we make no assumptions about the expected shape and evolution of the hydraulic fracture. By solving for focal mechanisms and activation stresses of field data, we anticipate to minimize the bias in the microseismic interpretation.

We envision that microseismic events occur in three general regions relative to the induced hydraulic fracture(s) (Figure 1):

1. Events that are adjacent to the parent hydraulic fracture, are likely to be related to leakoff of pressurized fluid from the fracture side-wall, and may occur in the zone of compressive stress shadowing (e.g., Pearson, 1981; Barree and Mukherjee, 1996; Ramurthy et al., 2007; Zoback et al., 2012) (Figure 1A).
2. Events caused by pervasive diffuse fluid flow in a critically stressed natural fracture network (Hennings et al., 2012). These events may indicate shear mechanisms regardless of the parent fracture origin that may be tensile (Figure 1B). The pressurization of the natural fracture network can generate
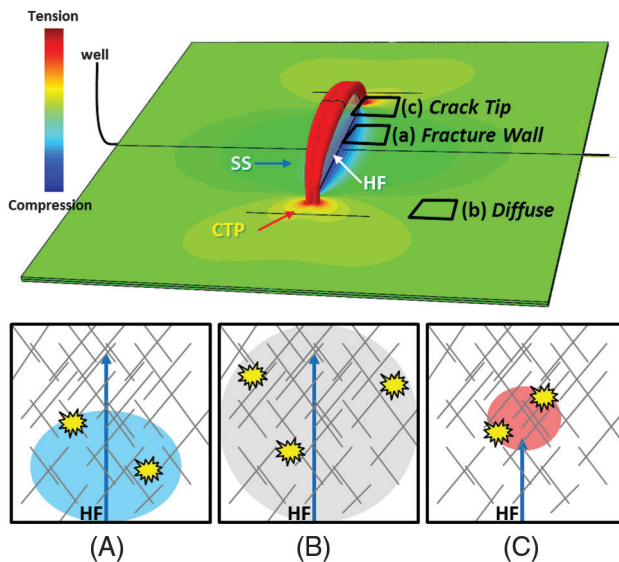
Figure 1. Concept model for microseismic activation. (Top) three-dimensional finite element stress model for an idealized planar, elliptical hydrofracture. Color contours indicate relative stress magnitude: warm colors are more tensile and cool colors are more compressive. Insets reflect prospective activation zones (A) adjacent to the hydrofracture (HF) walls in the stress shadow (SS), (B) diffusely spread around the hydrofracture in a natural fracture network, and (C) in the crack tip perturbation region (CTP).

structural permeability and fluid redistribution within the network (e.g., Sibson, 1996).

3. Events close to the hydraulic fracture tip, which is a zone of amplified stress field due the hydraulic fracture propagation (Figure 1C). The expected tensile, shear, and hybrid fractures (part 1, Busetti et al., 2014, this issue) facilitate the hydrofracture growth by linking the stress-induced fractures. This mechanism is akin to process zone mechanics during fault propagation (Reches and Lockner, 1994), brittle fracturing preceding fluidized pressure pulses in dikes (Baer, 1991), and tensile damage fracturing (Busetti et al., 2012).

We apply the approach previously described in this paper to a microseismic data set from the Mississippian Barnett Shale, Fort Worth Basin, which is a large unconventional gas field that requires hydraulic fracture stimulation to produce (Figure 2). It is widely recognized that the local structure, natural fractures, and the stress state affect the hydrofracture pattern in the Barnett Shale (e.g., Fischer et al., 2005; Daniels et al., 2007; Roth and Thompson,

2009). Gale et al. (2007) studied natural fractures in cores of Barnett Shale and concluded that preferential reactivation of the pre-existing fracture network could affect hydrofracture stimulations by redirecting fluid flow, a concept further investigated by Busetti and Reches (2007), Gale and Holder (2008), Busetti (2009, 2010), Kassis and Sondergeld (2010), Sil et al. (2012), and Zoback et al. (2012).

GEOLOGIC SETTING

Regional and Local Structures

The Fort Worth Basin is a north–south elongated foreland basin that formed in front of the Ouachita thrust belt during the late Paleozoic (Walper, 1982). The basin is bound by gentle arches (Figure 2), the most dominant being the Bend arch to the west, a broad north-plunging flexure and structural high thought to have formed as a hinge-line during Late Mississipian subsidence and when the basin tilted westward during the late Paleozoic (Pollastro et al., 2007). The northeast gently dipping (2–3°) regional structure coincides with the thickening of the Barnett Shale from 30 to 50 ft (9 to 15 m) thick at Llano uplift to ~1000 ft (~305 m) at Muenster arch. The reservoir consists of Mississippian sequences of heterogeneous mudstone (Singh, 2008) with low (hundreds of nanodarcys) matrix permeability (Mayerhofer et al., 2006). It lies below the Pennsylvanian Marble Falls Limestone and uncomfortably sits above heavily karsted Ordovician carbonates in the Viola Group in the northeast and the water-bearing Ellenberger Group to the southwest. The field includes minor northeast–southwest-striking high-angle normal faults and graben structures, and north–south striking faults associated with the Mineral Wells fault system in the northeast and the Ouachita structural front to the east (Figure 2) (Simon, 2005; Pollastro et al., 2007). Some of these faults were periodically reactivated and may be basement related (Montgomery et al., 2005). The dominant structural features in the field are the small flexures, faults, and fracture corridors related to karst collapse in the underlying Ordovician Ellenberger Group that pervade the Mississippian to Middle Ordovician strata (Hardage et al., 1996).

Figure 2. Map showing location of the Barnett Shale play and major structural features. Contour lines (interval = 1000 ft [305 m]) are for the top of the Ordovician Ellenberger group (Montgomery et al., 2005, used with permission of AAPG). The present study area in Denton County is indicated.
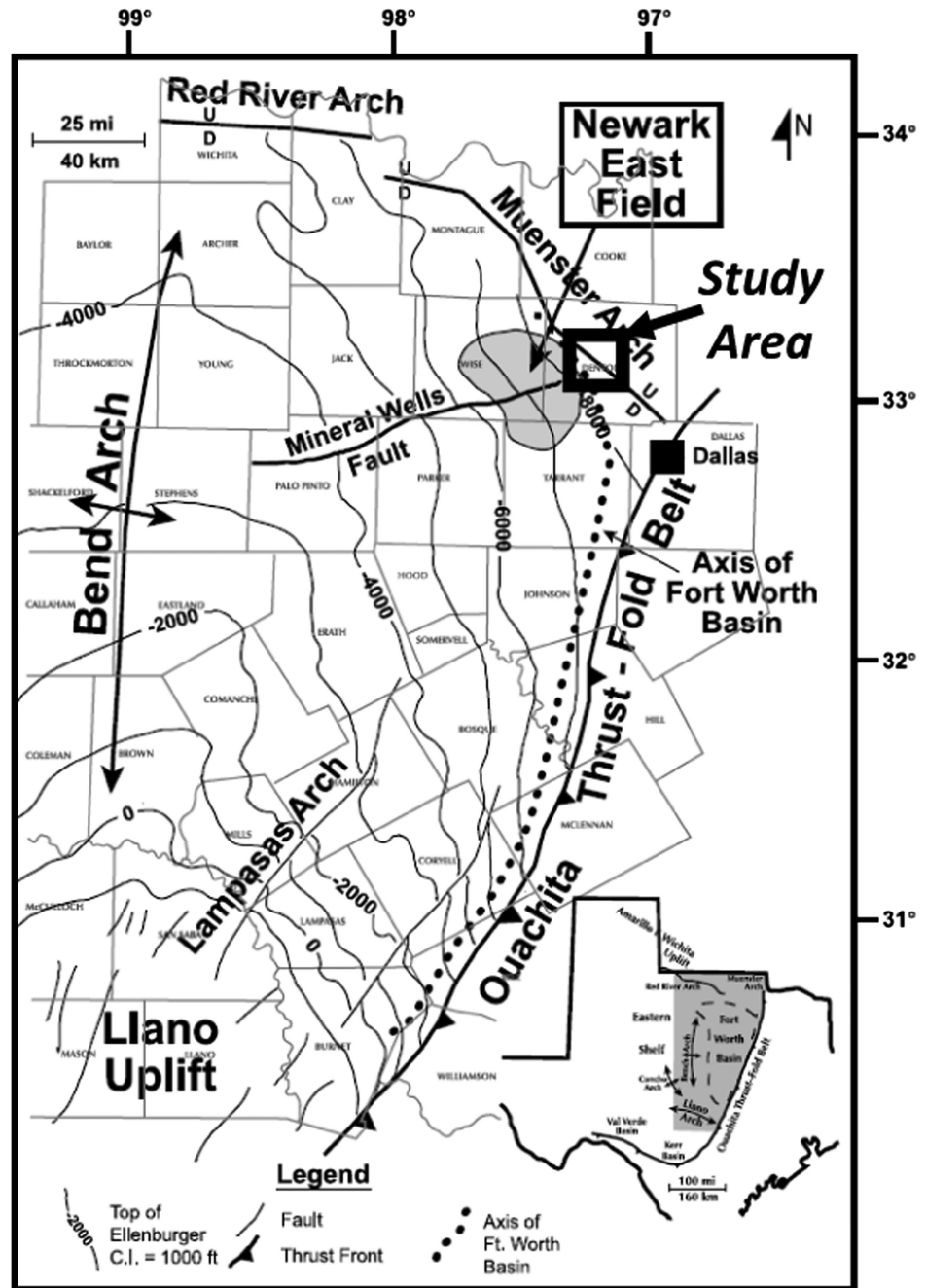
Local Control of the Structural Heterogeneity

The structural features (fractures, faults, folds) and current stress field in Barnett Shale were attributed to the following agents:

1. Collapse-related flexures, faults, and fracture corridors. For example, seismic interpretation in the southwestern part of the basin (Baruch, 2009)

indicated the presence of two dominant sets of lineaments (north–northwest and north–northeast) spaced 100–1000 ft (30.48–304.8 m) that originate from the underlying carbonate units, and locally extend upward past the overlying Marble Falls unit. The subvertical corridors form a coalescent rectilinear network of synformal sags, interpreted as collapsed paleocaves (Loucks, 1999; McDonnell et al., 2007; Baruch, 2009), some of

which may be related to basement-fault reactivation (Elibiju, 2009).

2. Lithologic variations that induce stress changes resulting from stiffness contrasts. At least nine distinct lithofacies have been identified from Barnett Shale cores (Singh, 2008), and four main subdivisions of the lower Barnett were described from log data for the study wells (Roy et al., 2014). Analyses of cores, borehole image logs, and gamma-ray logs indicated that the typical layer thickness is less than 1 m (<3 ft). Roy et al. (2014) suggested that carbonate fan bodies located near the present study area acted like a local fracture barrier.

3. Over-pressurization and pore-pressure variations. Estimates of the pore pressure based on the initial formation pressure during pump-in tests for a handful of wells studied by Busetti (2009) indicated a range of 0.489–0.524 psi/ft, which is consistent with the value of 0.52 psi/ft reported for the Barnett Shale in Montgomery et al. (2005).

Study Area

The study area (Figure 2) is located in Denton County, approximately 10 km (32,800 ft) southeast of the Muenster arch and Mineral Wells fault. Here, the Barnett Shale has four members (Roy et al., 2014): (1) a base unit is 12–15 m (39–49 ft) thick and is the most organically rich; (2) a 30-m (98-ft) thick sequence of siliceous mudstones with a few thin calcareous turbidites; (3) limestone beds up to several meters (tens of ft) thick that were interpreted as a smaller part of a larger carbonate-dominated submarine fan ("Stocker Fan") (Figure 3), the edge of the fan is marked by a facies transition that runs between the toe and heel of the two wells (Figure 3), where the
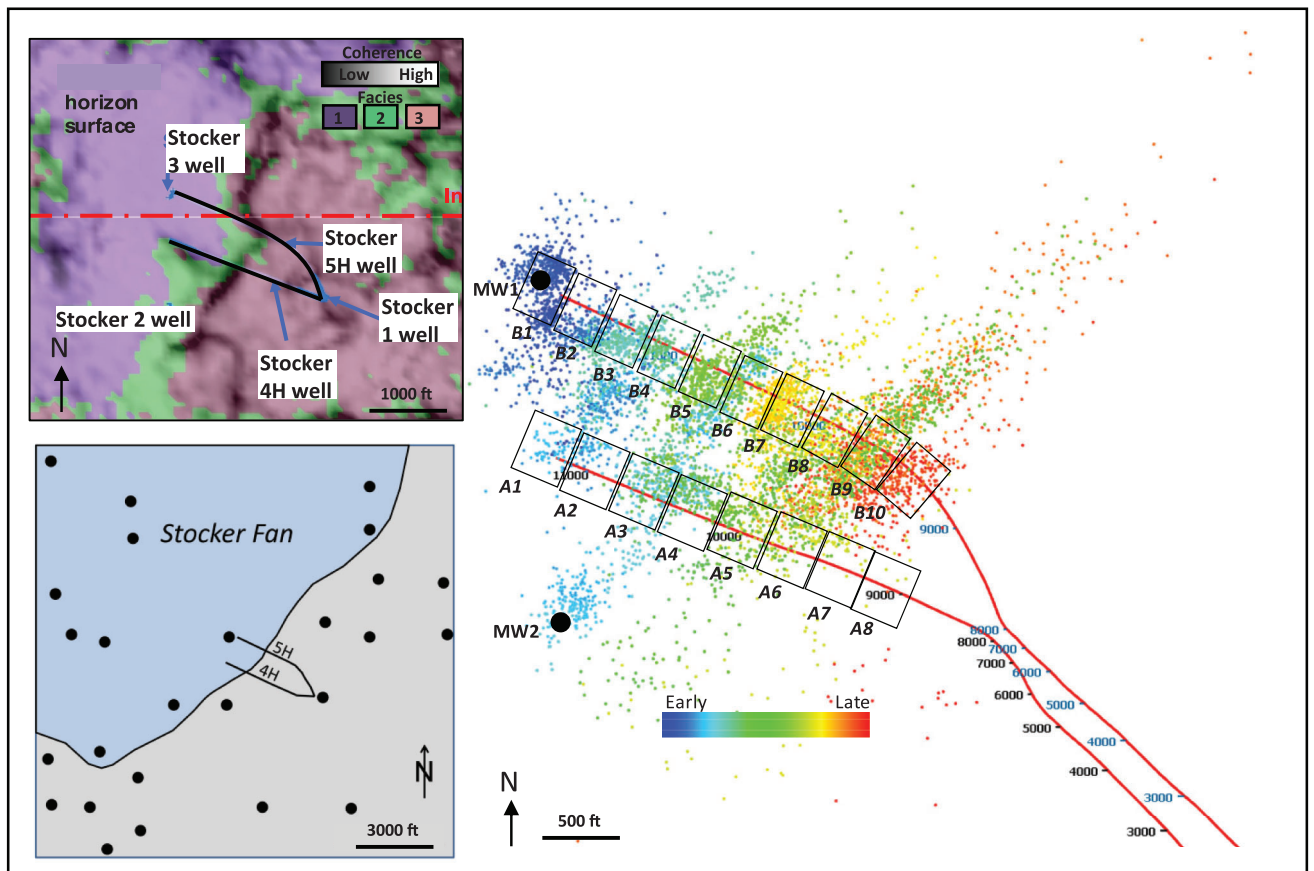
Figure 3. Maps of the study area and wells. (Top left) Co-rendering of seismic wavelet classification (colors) and coherence (shading); (Bottom left) cartoon showing location of the Stocker Fan. Black dots are vertical wells. Left images (Roy et al., 2014) used with the permission of AAPG/SEG. (Right) Study wells with relative locations of fracture stages shown as schematic black boxes and microseismic events plotted as dots. Dot color indicates event sequence. MW1 and MW2 are the two monitor wells.

fan and more calcareous beds are near the toes of the wells; and (4) the top unit is 120–130 m (393–427 ft) of interbedded limestones and siliceous mudstones, and was interpreted as a series of stacked carbonate submarine fan complexes (Roy et al., 2014).

We analyze the hydraulic fracturing in two horizontal wells, Stocker 4H and 5H (Roy et al., 2014, Sil et al., 2012, also insets in Figure 3), that are termed here as wells A and B, respectively. Image logs in the vertical, build, and lateral sections of well A were interpreted in detail for natural fractures by ConocoPhillips (R. Reid, 2010, personal communication). A total of 1246 fractures were picked in the Barnett interval, revealing a primary subvertical northeast–southwest set (n = 541, mean orientation = 036°/58.4° in right-hand rule strike/dip format), which was more clearly imaged in the horizontal section, whereas the more gently dipping fractures were picked in the build sections of the well (n = 663, mean orientation = 028°/64°). A secondary north–south fracture set was also imaged, consisting of about 100 nearly vertical fractures with strike between 150 and 180°.

Initial in Situ Stress for the Study Area

The preoperational in situ reservoir stress state was determined using drilling data (mud weight) and drilling-induced fractures (P. Paul, ConocoPhillips internal report). The analysis was based on 54 drilling-induced tensile fractures observed on image logs, and stress magnitudes were determined using the stress polygon technique (Zoback, 2007). Rock mechanics data were not collected on the study wells, and we used uniaxial strength data from core laboratory testing from an offset well. The calculated trend of the axis of maximum horizontal compression, S_{Hmax}, is 043°, and stress magnitudes are $S_v = 1.05$ psi/ft, $S_{Hmax} = 1.0$ psi/ft, $S_{Hmin} = 0.7$ psi/ft, and $P_p = 0.5$ psi/ft, in which S_v is the vertical, overburden gradient, which here is the maximum stress, σ_1; $S_{Hmax} \approx \sigma_2$; S_{Hmin} is the minimum horizontal stress gradient $\approx \sigma_3$; and P_p is the normal pore pressure gradient. Thus, the in situ stress state indicates normal faulting conditions with expected hydraulic fracture propagation toward azimuth 043°.

ANALYSIS APPROACH

The present analysis is based on 7444 microseismic events that were induced by hydraulic fracturing in two horizontal wells in the Barnett Shale (Figures 3, 4). In part 1, (Busetti et al., 2014, this issue) we used the source parameters and focal planes of these events to identify and separate shear, tensile, and hybrid source mechanisms based on two different source models (part 1, Busetti et al., 2014, this issue, Appendix 1), and to conduct stress inversion on the entire microseismic population (part 1, Busetti et al., 2014, this issue, Appendix 2). Here, we make a major change to the analysis and only the tensile source model that corrects fault plane orientation for tensile/compressive events is used for fault plane derivation following Vavrycuk (2001, 2011). It is expected that the fluid injection associated with hydraulic fracturing would activate shear fractures and hybrid events with mixed opening or closing modes (see part 1, Busetti et al., 2014, this issue).

The calculations are presented in the following scenarios:

1. Events activated by preoperational in situ stress
2. Events activated by stress inversion stress state
   a. Complete microseismic population (7444 events)
   b. Events stage-by-stage
3. Additional computations (Appendix)
   a. Detailed investigation of Stage B8 subpopulation
      i. Events as a function of distance from the wellbore
      ii. Events as a function of time/sequence of injection
   b. Activation stress as a function of friction

The first scenario ignores the stress inversion concept and instead considers the preoperational in situ reservoir stress state, assuming that regardless of stress perturbations induced by the hydrofracture, the preoperational in situ stress controls microseismic activation. In this case, the injected hydrofracture fluid (leaked-off) activates only fractures and faults that (1) are critically loaded by the tectonic stress state; and (2) intersect the hydrofracture (Barree and
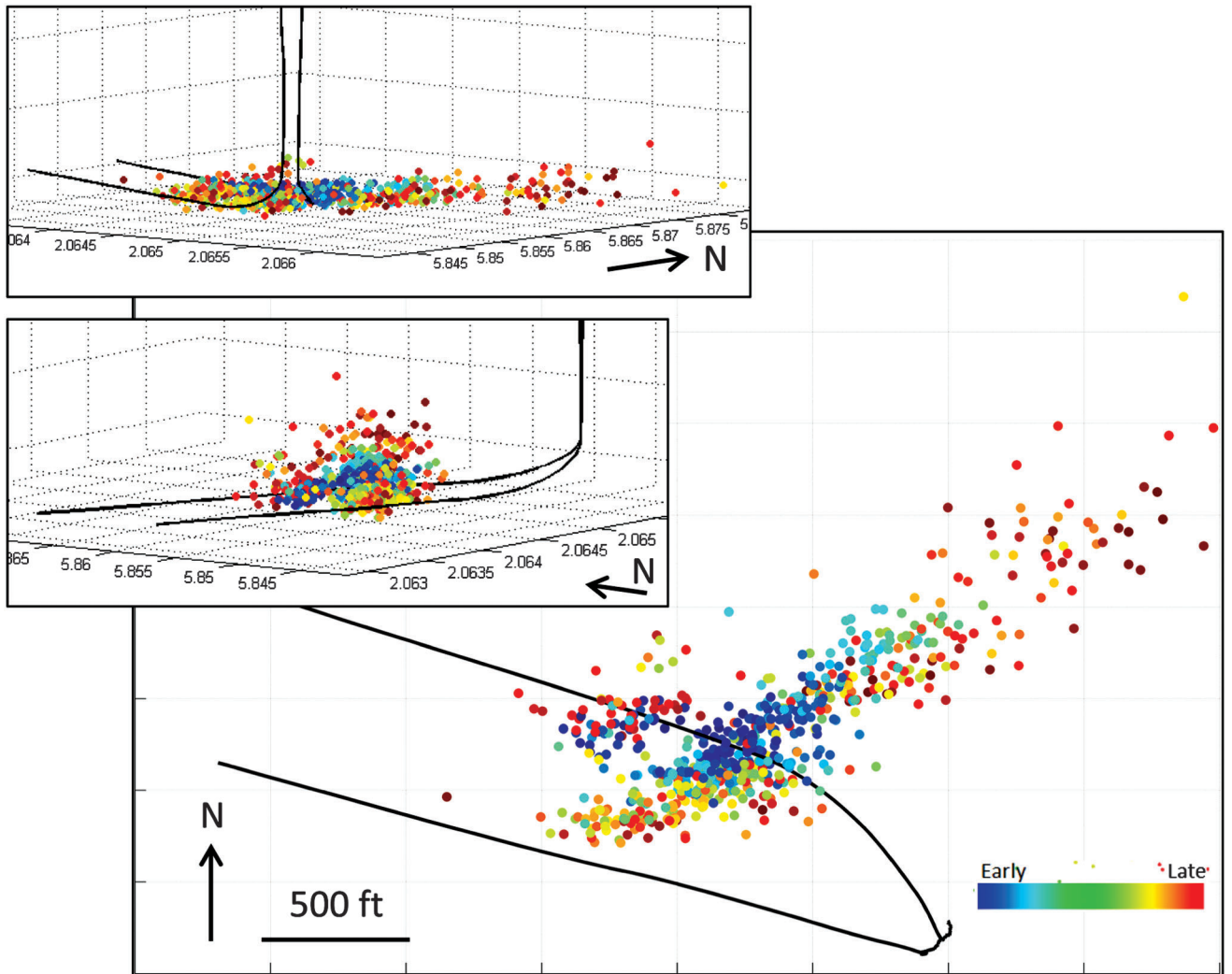
Figure 4. Map and three-dimensional views of stage B8 with microseismic events colored by event sequence. Grid spacing is 500 ft (152.4 m).

Mukherjee, 1996; Ramurthy et al., 2007; Zoback et al. 2012). For this case, we assume that the stress state is spatially uniform and equal to the preoperational in situ stress; the pore pressure may locally increase and activate the most critically stressed fractures caused by in situ stresses.

Scenarios 2a and 2b invoke the stress inversion of the microseismic events without assuming any controlling stress state. Instead, the fault activation is assumed to reflect the local stress state of a general stress field (Gephart and Forsyth, 1984; Leclere and Fabbri, 2013). To select the slipping fault plane of each pair of focal planes for a given microseismic event, we follow the procedure of part 1 and select the fault plane with the higher stress in the computed,

initial stress inversion; this selection is based on the critical pore fluid pressure, P_{critical}, (part 1, Busetti et al., 2014, this issue). Here, P_{critical} indicates the pore pressure required for shear failure to occur. A second stress inversion is then run on the selected faults to determine the activation stress state.

If the results of stress inversion calculations are similar to the preoperational in situ stress state, scenario 1 is supported, and preferential leakoff from the hydrofracture plane is the main activation mechanism. However, if the stress inversion results significantly differ from the in situ state, other mechanisms are required. Scenario 2a uses all of the microseismic events in the stress inversion, whereas in scenario 2b, the stress inversion is performed independently for

subsets of microseismic events grouped by each injection stage. If activation stress results for the individual hydraulic fracture stages (Figure 2) are similar to each other and to the stress state of all events (scenario 1b), then the results support geomechanical uniformity throughout the stimulation area, and vice versa if the stress results differ by subpopulation.
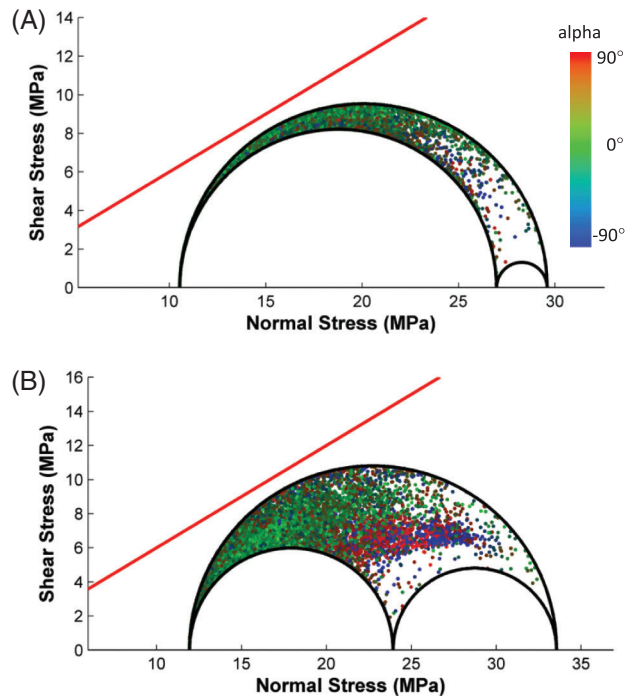
The additional scenarios (3a–3b) are provided in Appendix.

RESULTS

Solution Displays

The computation results are presented in a series of displays (Figures 5–8, A1) and in Table 1:

1. Mohr diagrams for scenarios 1 and 2a (Figure 5) using friction of $\mu = 0.6$ and cohesion $C = 0$.

Figure 5. Mohr diagrams for model configurations 1 and 2a with selected fault planes plotted. Blue dots indicate closing events α approaching -90°; green dots are $|\alpha|$ approaching 0°; and red dots are dilatant events α approaching 90°. The inclination angle α indicates the angle between the slip direction and the fault plane (see Busetti et al., 2014, this issue). Shear failure line is shown in red with coefficient of friction $\mu = 0.6$ and cohesion $C = 0$. (A) is the preoperational in situ stress state and (B) displays the computed stress state from stress inversion.

2. The three-dimensional (3-D) mean stress p' and deviatoric stress q for each case and as a function of friction (Figure 6), in which

$$p' = 1/3(\sigma_1 + \sigma_2 + \sigma_3) \qquad (1)$$

$$q = (1/2[\sigma_1 - \sigma_3]^2 + 1/2[\sigma_2 - \sigma_3]^2 + 1/2[\sigma_1 - \sigma_2]^2)^{1/2} \qquad (2)$$

3. Stereonets of the critical stress, $P_{critical}$, (Figures 7, 8) (Part I for definition).
4. Map of microseismic fault misorientation (Figure 9).
5. Computed stress as a function of distance from the wellbore and sequence for hydraulic fracture stage B8 (Figure 4 and A1).

Note that the calculations and Table 1 use the continuum mechanics convention of compression = negative; however for plotting purposes the Mohr diagrams and stereonets display compression = positive.

Stress Tensor Results

Stress Magnitude and Orientation

The magnitude of the primary stresses for the preoperational in situ stress state (scenario 1) and the activation stress state from inversion of all events (scenario 2a) are listed in Table 1 and displayed on Mohr diagrams in Figure 5A, B, respectively. The selected fault planes are plotted for each case. All faults are colored by the deviation angle α, the amount the slip vector deviates from pure in-plane motion (see Busetti et al., 2014, this issue). From Busetti et al. (2014, this issue), the faults with $|\alpha| > 60°$ generally correspond to vertical north–south oriented faults, whereas $|\alpha| < 60°$ corresponds to inclined northeast–southwest faults. For both scenarios, faults cluster toward the failure line. We expected the dilatant events (red) to cluster to the lower left. However, the opening, closing (blue), and pure shear (green) events occur in many orientations. For stress inversion case 2a (Figure 5B), there is a cluster of high $|\alpha|$ faults (normal stress of 20 to 25 MPa [2900 to 3626 psi]) that are misoriented in the stress field.

The orientations of the primary stresses are given by the eigenvectors of the stress tensor, Table 1, and vary depending on the fault population used in the
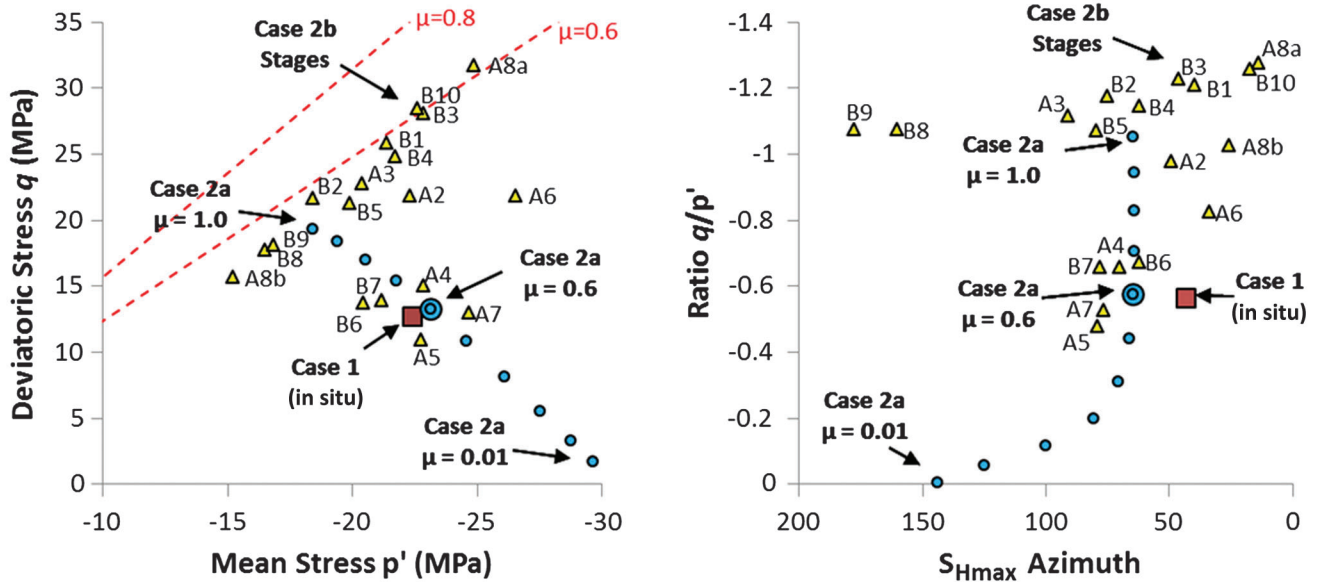
Figure 6. (Left) mean stress p' versus deviatoric stress q and (right) S_{Hmax} aximuth versus the ratio q/p'. The red square is the in situ preoperational stress state of Case 1a and the large blue circle is from stress inversion of all events in Case 1b. The yellow triangles are the stage-by-stage results for Case 2a with stage numbers labeled. The small blue circles are for Case 1b as a function of friction. The equivalent Mohr failure friction lines are plotted in dashed red lines for $\mu = 0.6$ and $\mu = 0.8$, in which $q = [6 \sin(\text{atan}(\mu))/(3 - \sin(\text{atan}(\mu))]p + (6 \cos(\text{atan}(\mu))/(3 - \sin(\text{atan}(\mu)))$.

stress inversion. Whereas the wellbore-derived preoperational in situ stress field assumes a vertical primary stress axis and indicates maximum horizontal stress of 043°, the computed stress fields are rotated in three-dimensions, with S_{Hmax} azimuth ranging from 014 to 178° stage-by-stage, or 065° for stress inversion using all events. The computed maximum primary stress, σ_1, for all cases indicates a normal faulting regime and is similar to the in situ state, but σ_1 deviates from vertical for nearly all of the inversion scenarios (Table 1) (i.e., the z-component of the eigenvector corresponding to σ_1 is less than 1). We interpret the deviation from the preoperational in situ state to indicate that the microseismic events activated under stress-perturbed conditions.

Stress Path Variables p' and q

Stress results in terms of mean and deviatoric stress, p' and q, are displayed in Figure 6. Parameters p' and q are similar to shear and normal stress on a Mohr diagram (Figure 5), but include dependency of the intermediate stress. Points upward and to the left indicate relative proximity to fail in shear; points lower and to the left indicate relative proximity to fail in tension. Figure 6 shows the results for each

scenario, in which the preoperational in situ stress state of case 1 is plotted as the red square, case 2a is the large blue circle, and the yellow triangles are the stage-by-stage results of scenario 2b. The small blue dots are for scenario 2a as a function of friction, which is discussed in Appendix. The preoperational in situ stress state of case 1 and the full-population stress inversion stress field of case 2a have very similar results in p'-q space (Figure 6), for example, similar propensity to fail, but the stress orientation and magnitudes differ (Table 1, Figure 5). Scenarios 1 and 2a have high mean stress and low deviatoric stress and are the most stable fields, along with stages A4, A5, A7, B6, and B7, which form a group located near the center of both wells that have similar activation stress states (Table 1 and Figure 7). The remaining stages form a nearly linear trend in p'-q space (e.g., A8b, B8, B9… A8a; Figure 6) that generally coincides with the prescribed Mohr failure line (dashed red line in Figure 6; the relationship between the failure line in Mohr and p'-q space is given as

$$q = [6 \sin(\text{atan}(\mu))/(3 - \sin(\text{atan}(\mu))]p$$
$$+ [6 \cos(\text{atan}(\mu))/(3 - \sin(\text{atan}(\mu))], \quad (3)$$
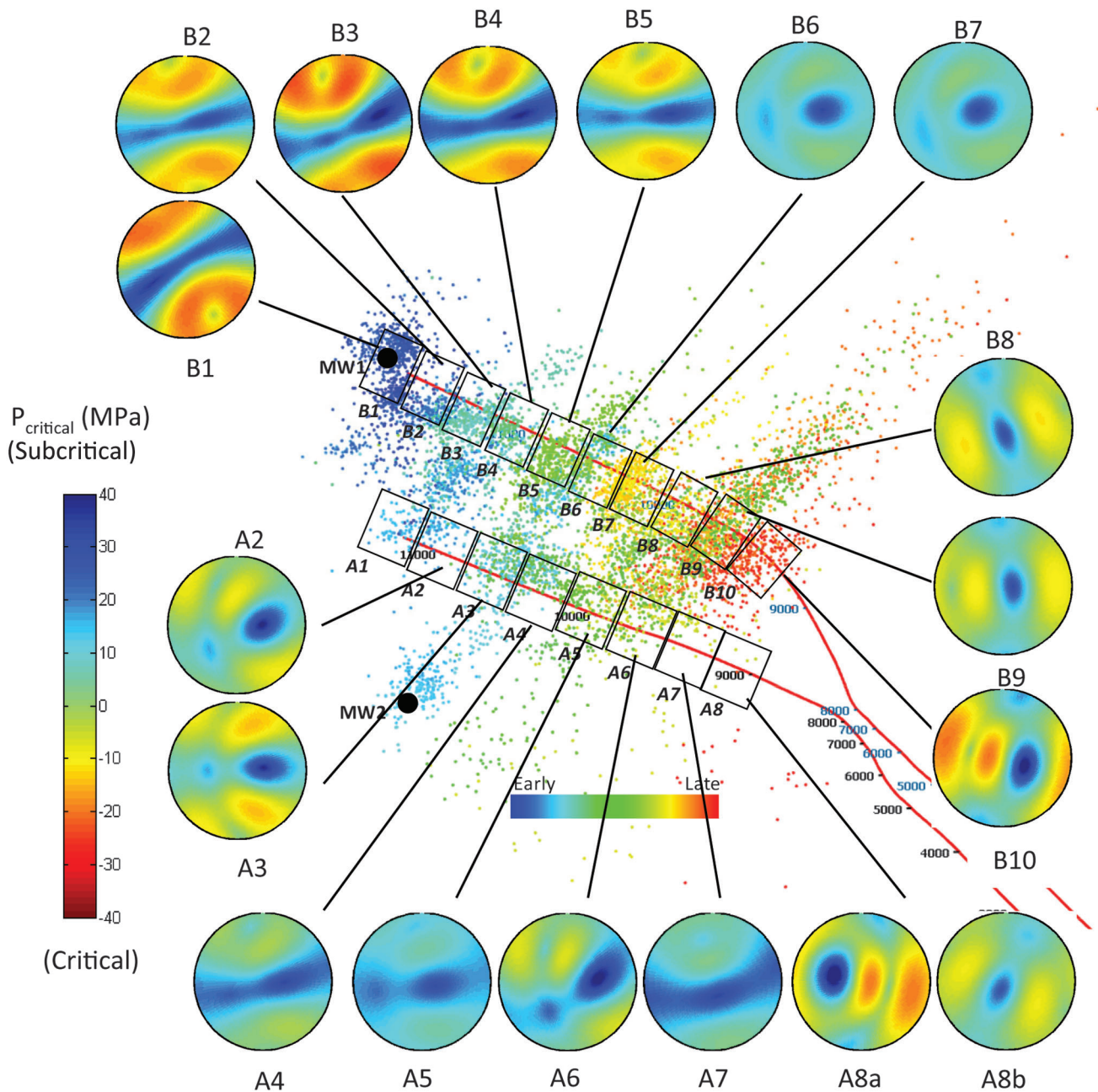
Figure 7. Microseismic map with overlay of $P_{critical}$ stereonet plots for each stage. Fluid pressure required for shear failure is plotted, using the configuration of Case 4 stress inversion on a stage-by-stage basis.

in which μ and C are the friction coefficient and cohesion in Mohr space).

Regional Stress Heterogeneity

Activation Stress Stage-by-Stage

We applied stress-inversion calculations on all 18 hydro-fracture stages, A2–A8 and B1–B10 (scenario 2a).

The results (Table 1) are graphically presented by the calculated the stress tensor, p' and q, (Figure 6), and the critical pore pressure $P_{critical}$ stereoplots (Figures 7, 8). Table 1 and the p'-q plot in Figure 6 capture the range in stress magnitudes for each injection stage, marked as the yellow triangles in Figure 6. Calculated pressure stress p' ranges from −15.2 to −26.5 MPa; deviatoric stress q ranges from
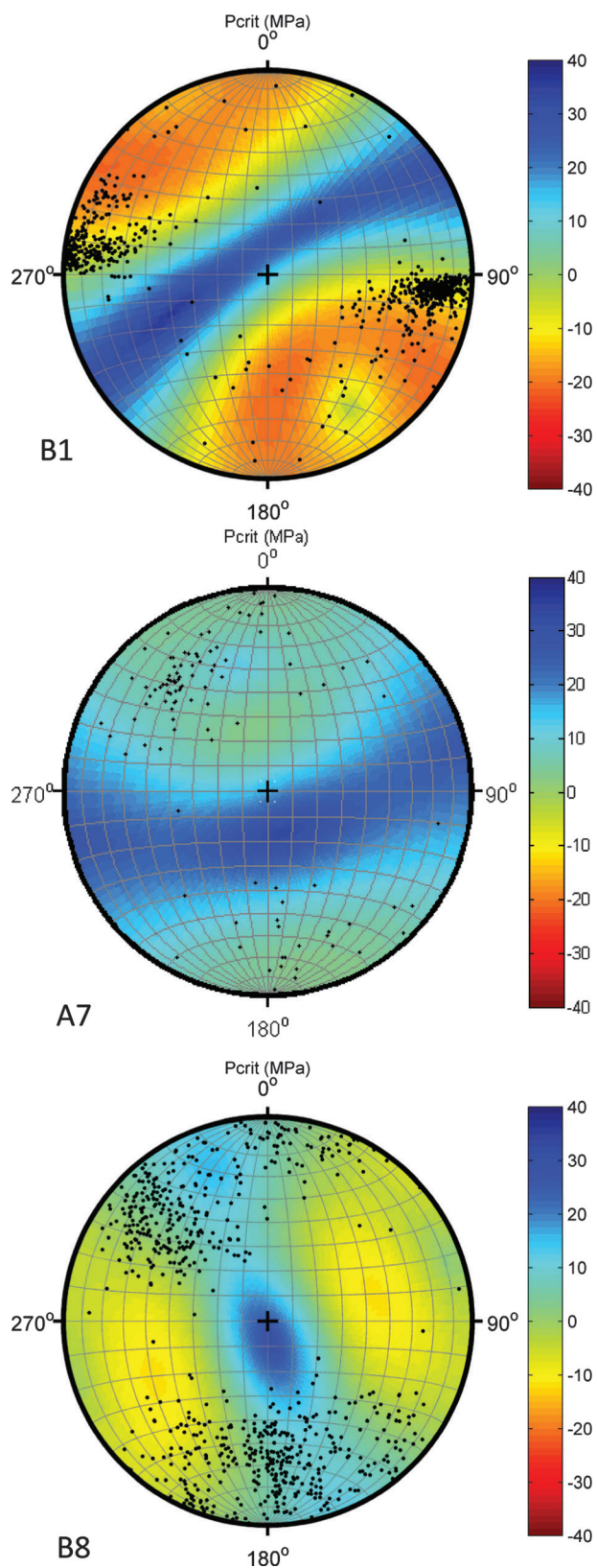
Figure 8. $P_{critical}$ stereonet plots for stages B1 (top), A7 (middle), and B8 (bottom), with overlays of fault populations for each stage.

to 10.9 to 31.8 MPa (1580.9 to 4612.1 psi) (note stage A1 gives anomalous stress results).

We present the $P_{critical}$ results on stress stereonets (e.g., Zoback, 2007) for each stage in map view (Figure 7), as well as $P_{critical}$ and fault orientations for stages B1, A7, and B8 (Figure 8). The $P_{critical}$ value is the pore pressure that is required to allow slip on a given fracture subjected to a given stress state. Here, $P_{critical}$ was solved for all possible fault orientations from $0° \leq$ strike $\leq 360°$ and $0° \leq$ dip $\leq 90°$, plotted as poles to planes in stereonet view (Figures 7, 8). Red shading indicates orientations of unstable faults whereby the activation stress state is near or, in some cases, exceeds the shear failure criteria. Blue colors indicate orientations of stable faults that require reduced σ_3 to slip. Computed stress for each stage differs and the only systematic trend is that for most stages, σ_1 is inclined from vertical and σ_2 lies in the northeast–southwest quadrants. Stress fields from stages B1, B2, B3, B4, and B5 are oriented similarly and they indicate a considerable part of the potential range of fault orientations to be critically stressed by as much as 20–30 MPa (2900 to 4351 psi) (orange-red zones, Figure 7). Stages A2 and A3 also indicate critical state of 10 MPa (1450 psi) (yellow zones, Figure 7). An abrupt change in pattern appears between stages B5 and B6 and A3 and A4, and between stages A7 and A8 and B7 and B8. The stages closest to the heels of the wells also have a similar stress field, with more north–south oriented σ_2, and are more critically stressed (yellow-orange zones, Figure 7).

Fault Misorientation

We plotted interpolated critical stress results for each stage in map view in Figure 9 to view domains of fault misorientation. The technique was adopted from Leclere and Fabbri (2013) who used focal mechanisms, stress inversion, and critical stress concepts to investigate fault reactivation associated with the 2011 Tohoku-Oki earthquake, Japan. The procedure involves plotting each microseismic event on the map, colored by instability parameter, $P_{critical}$, and then interpolating the points. Whereas critical stress stereonets (Figures 7, 8) highlight differences in the computed stress field, the map in Figure 9 shows which faults in the field are optimally oriented and

Table 1. Results Summary by Stage ($\mu = 0.6$, $C = 0$)

Stage	Number of Events	Stress Tensor (MPa)			Stress Direction (Eigenvector)			Stress Path Variable		
		σ_{i1}	σ_{i2}	σ_{i3}	$\sigma_{1\text{-vec}}$	$\sigma_{2\text{-vec}}$	$\sigma_{3\text{-vec}}$	AZ S_{Hmax}	p'	q
N/A (Case 1a)	N/A	−18.2	−8.2	0.0	0.00	0.68	−0.73	43.0	−22.4	12.7
	preoperational	−8.2	−19.3	0.0	0.00	0.73	0.68			
	in situ stress	0.0	0.0	−29.6	1.00	0.00	0.00			
ALL (Case 1b)	7444	−13.8	−2.8	3.5	−0.07	0.38	−0.92	64.5	−23.1	13.3
		−2.8	−25.6	−5.2	0.53	0.80	0.29			
		3.5	−5.2	−30.0	0.85	−0.46	−0.26			
A1 (Case 2a)	13	−6.2	−10.9	186.1	−0.68	0.04	−0.73	87.6	−21.8	229.1
		−10.9	−29.0	−7.9	−0.01	1.00	0.07			
		186.1	−7.9	−30.1	0.73	0.05	−0.68			
B1 (Case 2a)	754	−8.1	−15.1	−5.3	−0.30	0.47	0.83	39.7	−21.4	25.8
		−15.1	−26.1	7.1	−0.78	0.39	−0.50			
		−5.3	7.1	−30.0	0.55	0.80	−0.24			
B2 (Case 2a)	297	−0.1	−6.1	0.3	0.10	0.21	0.97	75.2	−18.4	21.7
		−6.1	−25.3	−4.3	0.56	0.80	−0.23			
		0.3	−4.3	−29.8	0.82	−0.57	0.04			
A2 (Case 2a)	619	−10.3	−3.5	3.5	−0.01	0.55	0.84	49.2	−22.3	21.8
		−3.5	−26.6	−13.5	0.66	0.63	−0.40			
		3.5	−13.5	−30.0	0.75	−0.55	0.37			
A3 (Case 2a)	278	−3.2	−1.2	−1.6	0.05	−0.01	1.00	90.8	−20.4	22.8
		−1.2	−28.0	−10.9	0.67	0.74	−0.03			
		−1.6	−10.9	−29.9	0.74	−0.67	−0.05			
B3 (Case 2a)	686	−4.7	−12.1	5.3	0.18	−0.42	−0.89	46.0	−22.8	28.1
		−12.1	−33.9	−10.0	0.82	−0.43	0.37			
		5.3	−10.0	−29.9	0.54	0.80	−0.26			
B4 (Case 2a)	251	−2.1	−4.7	7.2	−0.02	−0.32	−0.95	61.8	−21.7	24.8
		−4.7	−33.2	−6.8	0.78	−0.60	0.18			
		7.2	−6.8	−29.8	0.63	0.73	−0.26			
A4 (Case 2a)	467	−10.9	−3.1	3.2	0.03	−0.29	−0.96	70.0	−22.8	15.0
		−3.1	−27.4	−4.6	−0.58	−0.79	0.21			
		3.2	−4.6	−30.2	−0.81	0.55	−0.19			
A5 (Case 2a)	712	−14.6	−0.5	2.7	−0.13	0.18	0.97	78.9	−22.7	10.9
		−0.5	−23.6	−3.4	0.37	0.92	−0.12			
		2.7	−3.4	−30.0	0.92	−0.35	0.19			
B5 (Case 2a)	534	−1.6	−0.5	4.6	−0.10	0.14	0.99	79.7	−19.9	21.3
		−0.5	−28.1	−5.6	0.62	0.78	−0.05			
		4.6	−5.6	−29.9	0.78	−0.61	0.16			
B6 (Case 2a)	331	−12.4	−0.8	0.6	−0.01	0.18	0.98	77.9	−21.2	13.9
		−0.8	−21.2	−7.1	0.48	0.86	−0.16			
		0.6	−7.1	−30.0	0.87	−0.48	0.10			
A6 (Case 2a)	344	−16.7	−6.4	4.3	0.07	0.68	0.73	33.5	−26.5	21.9
		−6.4	−32.8	−13.6	0.75	0.45	−0.48			
		4.3	−13.6	−30.1	0.66	−0.58	0.48			

Table 1. Continued

Stage	Number of Events	Stress Tensor (MPa)			Stress Direction (Eigenvector)				Stress Path Variable	
		σ_{i1}	σ_{i2}	σ_{i3}	$\sigma_{1\text{-vec}}$	$\sigma_{2\text{-vec}}$	$\sigma_{3\text{-vec}}$	AZ S_{Hmax}	p'	q
A7 (Case 2a)	107	−17.2	−2.1	7.7	−0.40	0.23	−0.88	76.5	−24.6	13.0
		−2.1	−26.5	−2.0	0.13	0.97	0.20			
		7.7	−2.0	−30.2	0.91	−0.03	−0.42			
B7 (Case 2a)	743	−12.7	−1.6	0.9	−0.01	0.44	0.90	62.0	−20.5	13.8
		−1.6	−18.7	−6.7	0.42	0.82	−0.39			
		0.9	−6.7	−30.0	0.91	−0.38	0.19			
B8 (Case 2a)	698	−15.7	4.5	3.2	−0.21	0.92	−0.32	160.4	−16.5	17.7
		4.5	−3.6	0.6	0.01	−0.33	−0.94			
		3.2	0.6	−30.2	0.98	0.20	−0.06			
A8-a (Case 2a)	7	−17.7	2.8	−6.0	−0.17	0.97	0.17	13.7	−24.9	31.8
		2.8	−27.9	24.3	0.68	0.24	−0.69			
		−6.0	24.3	−29.0	−0.71	0.00	−0.70			
B9 (Case 2a)	480	−15.3	0.9	0.6	−0.05	1.00	0.06	177.5	−16.9	18.1
		0.9	−5.2	−7.7	0.27	−0.04	0.96			
		0.6	−7.7	−30.1	0.96	0.06	−0.27			
B10 (Case 2a)	103	−19.6	1.0	7.2	−0.22	0.95	−0.20	17.3	−22.6	28.4
		1.0	−18.1	−21.0	0.57	0.30	0.76			
		7.2	−21.0	−30.1	0.79	0.06	−0.61			
A8-b (Case 2a)	20	−12.8	−5.1	3.0	−0.24	0.86	0.45	25.9	−15.2	15.6
		−5.1	−5.7	2.8	−0.17	0.42	−0.89			
		3.0	2.8	−27.2	0.95	0.29	−0.05			
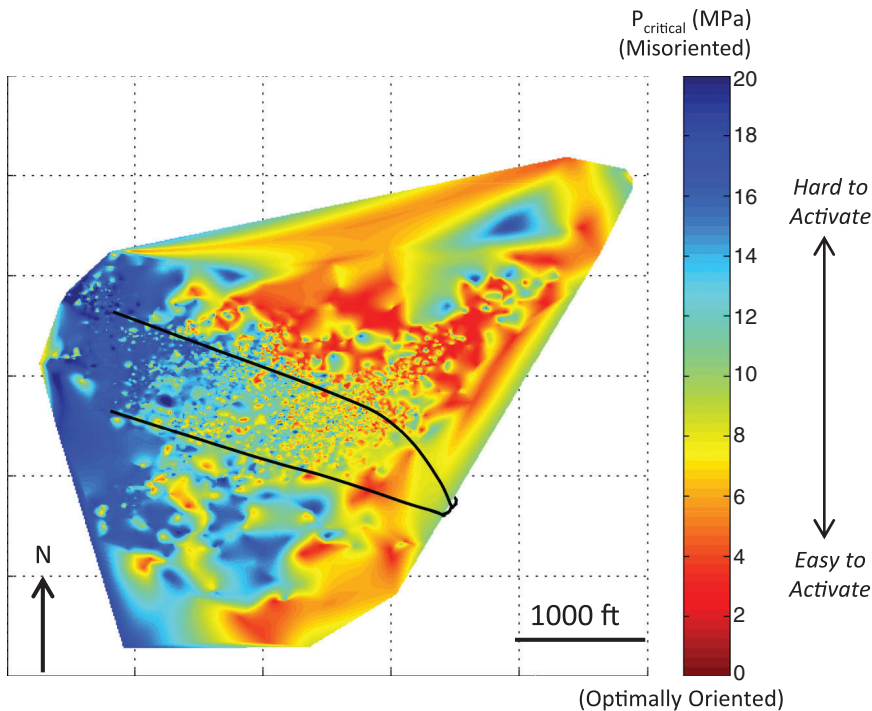
Figure 9. Interpolated map of instability parameter $P_{critical}$ for every microseismic event, for the configurations in Case 2a of stress inversion stage-by-stage. Blue zones reflect faults that are misoriented in the activation stress field, whereas red zones are optimally oriented.

more easily activated (orange zones in Figure 9), compared to those that are subcritically stressed and misoriented in the stress field (blue zones in Figure 9). For example, the more red colored stereonet (unstable) of stage B1 relative to the blue stereonet (stable) of stage A7 in Figure 8 is because of stage B1's higher deviatoric stress (25.8 vs. 13.0 MPa [3741.9 vs. 1885.4 psi] for A7). On the misorientation map (Figure 9) B1 is in a blue subcritical zone and A7 in a red zone. Because faults in B1 are misoriented (blue in Figure 9), they required a more critical stress state to activate (yellow-red zones of the stereonet in Figure 8), whereas faults in A7 are more optimally oriented (red in Figure 9) and were able to activate under a more weakly stressed condition (green-blue in Figure 8). Stage B8 reflects a mixed case (faults lie in both yellow and blue zones in Figure 8). The zonation displayed in Figures 7, 9 appears to agree with the local geology: (1) the carbonate fan geometry (Stocker Fan, Figure 3) coincides with the blue zones of misorientation at the toes of the wells (Figure 9) and (2) the green seismic wavelet classification-based facies (top inset, Figure 3) bounded by the low seismic coherence trend (gray shaded area of Figure 3) is approximately in the same location as the sharp change in activation stress character between stages A3 and A4 and B5 and B6 (Figure 7).

DISCUSSION: LOCATION OF THE MICROSEISMIC EVENTS RELATIVE TO HYDROFRACTURES

In part 1 (Busetti et al., 2014, this issue), we interpreted two activated fault sets: inclined northeast–southwest fault planes with low $|\alpha|$ and vertical north–south planes with high $|\alpha|$. These orientations are consistent with local wellbore natural fracture orientations and with regional structural trends. For this data set, it was not possible to directly link microseismic patterns to local structural features such as seismic-interpreted faults or fracture corridors due to the seismic resolution. Direct correlation of microseismic events to the fractures observed in wellbore image data (for example, by projecting microseismic event density back to the wellbore for comparison against wellbore fracture count) is also highly problematic,

as it is unlikely that many natural fractures extend continuously along strike for the full length of the microseismic events cloud. Nonetheless, we believe the similarity in the orientation of the focal planes to the observed local and regional fracture and fault data to be compelling evidence for the microseismic events signaling activation of pre-existing discontinuities.

There also appears to be a reasonable correlation of the microseismic behavior with geological facies changes and activation stress domains (Figures 3, 7, 8). Additional investigations on the data set (Roy et al., 2014), which include a range of ConocoPhillips internal reports, identify positive correlation between lateral changes in microseismic event distribution and density with seismic coherence and curvature attributes, distributed temperature sensing, production log data, and time-lapse seismic anomalies (A. Mironova, 2013, personal communication). For example, using a geocellular model (Petrel, Schlumberger) with 3-D carbonate facies interpreted from seismic acoustic impedance and log-derived gamma ray cutoffs, the interpreted Stocker Fan and other potential carbonate lobes were found to separate zones of upwardly decreasing microseismic event count (assumed to act as minor impediments to fracture growth) (R. Treverton, 2012, personal communication). Though the relationship between interpreted local geological heterogeneity, microseismicity, and geomechanical behavior is complicated and still not fully understood, it appears that more thorough reconciliation with the other available geologic, geophysical, and operational data (pressure history, rock mechanical properties, etc.) is possible. Synthesis of all the available data is outside of the present scope, and thus we return the discussion to investigation of where microseismic activation occurs relative to the hydrofractures.

Three general settings were assumed for the microseismic activation (Figure 1): (1) adjacent to a major hydraulic fracture in the stress-shadowing region, (2) far away from the fracture but in some area of weak mechanical disturbance, and (3) ahead of a hydraulic fracture, near the crack tip region (note that although the figure depicts an idealized symmetric bi-wing fracture, fracture mapping of the events in real-time and 3-D suggests more irregular patterns: we do not suggest the idealized geometry to reflect the

actual hydraulic fractures in this data set). We summarize our findings below.

The computed activation states from stress inversion indicate increase in deviatoric stress, and decrease in mean stress and stress rotation. We understand the activation stress state to be the combined effect of both the in situ stress and the perturbed stress field caused by hydraulic fracturing. Thus, the microseismicity of the present data is interpreted as predominantly induced instead of triggered, such that events were caused by significant disturbance to the in situ stress state. This finding also requires that the microseismicity was not induced from pore pressure change alone. The concept of fluid leakoff because of shifting in situ stress circles on a Mohr diagram to the left with increasing injection pressure but without changing the size of the circles is an unlikely cause of the microseismicity. Instead, a hydromechanical mechanism that explains hybrid (mixed tensile, compressive, and shear mode) events in the presence of a perturbed stress field is required. It is also unlikely that the microseismic events occurred in the stress shadowing region adjacent to the hydrofracture walls, an area of stress rotation and elevated compressive stress (Sneddon, 1946; Roussel and Sharma, 2011, 2012), because nearly all of the stress inversion results indicate a reduction in mean stress. We conclude that locations 1 and 2 previously described in this paper (Figure 1A, 1B) are unlikely locations for the microseismic activity.

Fault activation near the crack tip (Figure 1C) is compatible with the stress inversion results. Hybrid and shear failure in the tensile stress perturbation zone ahead of propagating crack tips were described in detail (e.g., Pollard and Segall, 1987; Baer, 1991; Reches and Lockner, 1994; Healy et al., 2006) and involves stress rotation, reduction of mean stress, and increased deviatoric stress. In finite element simulations of hydraulic fracture segment propagation, Busetti et al. (2012) found that regions of rock slightly off-plane to the propagating crack path experience up and leftward directed stress paths in p'-q space, similar to the activation stress paths that can be inferred from Figure 6. Healy et al. (2006) studied stress perturbations around penny shape cracks and recognized a domain of enhanced shear activation that extends some distance ahead of propagating

crack tips and at an angle oblique to the far-field S_{Hmax} axis. The sequence of induced damage, coupled with fracture growth and sustained flow, could cause complex sequence dynamic pressure pulses resulting in both opening and closing events (see discussion in part 1, Busetti et al., 2014, this issue). Dynamic hydromechanical behavior occurring ahead of the crack tip explains microseismic fault activation and hydraulic fracture growth, but implies that the hydraulic fracture propagates into a locally disturbed region containing microseismicity, instead of the other way around. A mechanism in which hydromechanical pressure pulses ahead of the hydrofracture tip activate oblique faults, and natural fractures may allow proppant emplacement into fracture orientations that would otherwise remain closed under usual leakoff conditions (e.g., at the fracture walls). This mechanism supports the notion that sustained permeability enhancement is possible for fractures activated in shear, which are generally accepted to be the primary elements of the stimulated rock volume.

CONCLUSIONS

A method was developed to find the activation stress conditions during hydraulic fracturing based on microseismic events data. The approach involves determining earthquake focal mechanisms and potential fault planes, and then applying geomechanical techniques of critical stress (instability) and stress inversion. A product is the full activation stress tensor for any microseismic subpopulation of the stimulated rock volume. The present approach depends on multiple monitor wells and advanced microseismic processing techniques.

The main findings are (1) derived microseismic fault orientations indicate the microseismic events correspond to one of two fault sets that are consistent with other observed structural trends in the Barnett; (2) activation stresses indicate significant mechanical perturbations that are consistent with locations obliquely ahead of hydrofracture tips; (3) activation stresses are incompatible with the stress shadow region adjacent to hydrofractures: for example, sidewall leakoff does not appear to be a viable

mechanism for the microseisms; (4) significant geo-mechanical heterogeneity occurs stage-by-stage; (5) the most highly misoriented microseismic faults (those that require more energy to activate) occur near the toes of the wells in the same vicinity as the carbonate-dominated Stocker Fan feature.

APPENDIX: ADDITIONAL CALCULATIONS

Fault Population Subsets

In addition to the two main scenarios previously described in this paper (1, 2A, 2B), we investigated a third case of subpopulations (3a) that sort stage B8 events (Figure 4) into 10 smaller subsets. Scenario 3ai addresses whether the activation stress state responsible for near wellbore events is different from that of the distant events, for instance, caused by more pressure interference near the wellbore. Next, scenario 3aii groups the events by time-sequence to determine whether early events reflect different stress conditions than later events, for example, early fracture extension versus late in-filling events. For comparison, we also grouped the events into 10 subsets sorted randomly. To answer these subset questions, we calculated activation stress using fault subpopulations for stage B8. We selected the B8 hydraulic fracture stage because it formed the longest microseismic cloud (Figures 3, 4). Events were grouped into 10 subsets giving 30 independent stress inversions. The first category is by distance from the wellbore, measured from the middle of the stage B8 perforation clusters (green triangles, Figure 10, top), the second by event sequence or time (red squares, Figure 10, top), and for comparison a third subset comprises all the stage B8 events sorted randomly and then is divided into 10 subsets (blue diamond, Figure 10, top). Results show no clear trend between distance or event sequence and S_{Hmax} azimuth, or mean or deviatoric stress, p' or q. Distance and sequence yield no better trend than the randomized data set. Variability in activation stresses relating to fracture in-filling versus spreading events or changes in the pumping cycle is not evident from the present analysis. However, plotting the sequence and distance subsets against each other (e.g., S_{Haz} for the nearest 10% of events vs. S_{Haz} for the earliest 10%) shows a nearly 1:1 relationship (Figure 10, bottom), indicating that despite a heterogeneous (or noisy) activation stress state, stage B8 events generally spread outward with time.

Effects of Material Properties

The stress inversion technique used in this study is based on solving the inverse problem for the Coulomb failure criteria, and thus depends on friction angle. Up to this point, we assumed a friction coefficient of 0.6. We repeated the stress inversion for all 7444 events of scenario 2a, for the range $0.01 \leq \mu \leq 1.0$. Results indicate that lowering friction results in σ_1 being more inclined from vertical and σ_2 and σ_3 also rotate clockwise (increasing S_{Hmax} azimuth) (Figure 6, right). In p'-q space (Figure 6, small blue dots),
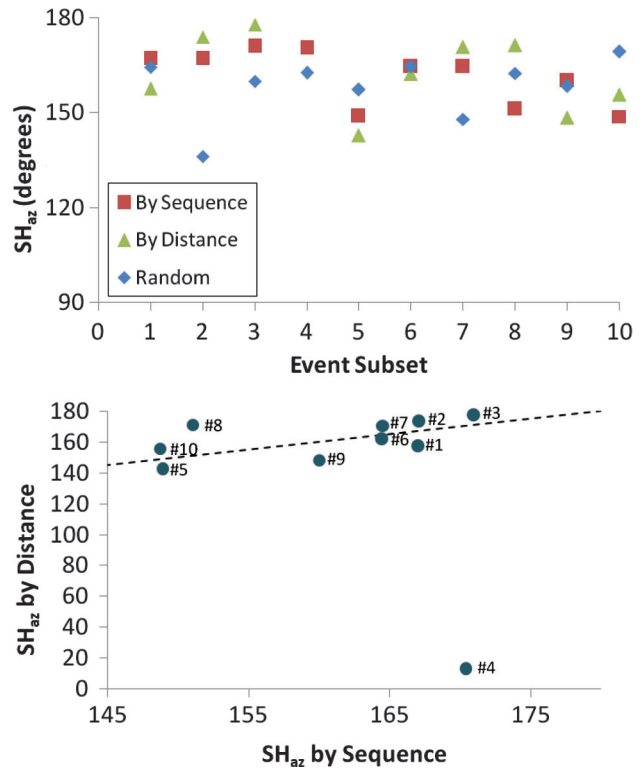
Figure 10. (Top) Computed maximum horizontal stress direction, S_{Haz}, as a function of well B8 microseismic event subpopulations. By sequence (red squares), early events are to the left and late events are to the right. By distance (green triangles), events near the wellbore are to the left and distant events are to the right. Random subsets (blue diamonds) reflect 10 randomly sorted event subsets. (Bottom) Maximum horizontal stress direction, S_{Haz}, by sequence versus S_{Haz} by distance, in which 1 indicates the subsets earliest and nearest to the wellbore. The dashed black line indicates a 1:1 correlation.

the effect of decreasing friction is to raise the mean stress and lower deviatoric stress. The ratio of q/p' decreases linearly with reduced friction. We view the dependency of stress orientation and magnitude on friction as an intrinsic uncertainty of the problem that should occur because of lithologic variations. For example, $\mu = 0.4$–0.8 reflects measured values of friction for different Barnett Shale samples (Zoback et al., 2012). We also calculated the misfit angle as a function of friction angle, in which the misfit angle $\alpha_{misfit} = \cos^{-1}(\tau \cdot S)$ is the angle between the unit shear stress direction τ and the unit slip direction S, and · indicates the dot product. Misfit for scenario 1a, in which faults were picked a priori from the preoperational in situ stress state, has little dependency on friction. When stress inversion is used, misfit decreases to zero as friction approaches zero. These findings agree with the conclusions of Reches (1987) that misfit minimization methods imply $\mu = 0$. It was recognized that minimized misfit may not represent actual fault motion. For example, the method of Angelier (2002, p. 589) appeals to numerical simulations by Dupin et al. (1993) and explains that "slip occurs on some faults despite a large angle between the slip vector and

the shear stress as a consequence of geometrical requirements in the faulted blocks." Using the methods of this study, a larger degree of misfit must be tolerated if high friction values are assumed.

REFERENCES CITED

Angelier, J., 2002, Inversion of earthquake focal mechanisms to obtain the seismotectonic stress IV—a new method free of choice among nodal planes: Geophysical Journal International, v. 150, no. 3, p. 588–609.

Athavale, A. S., and J. L. Miskimins, 2008, Laboratory hydraulic fracturing tests on small homogeneous and laminated blocks: American Rock Mechanics Association 2008 Symposium, ARMA 08-067, the 42nd US Rock Mechanics Symposium and 2nd US-Canada rock Mechanics Symposium, San Francisco, California, June 29–July 2, 2008, 9 p.

Baer, G., 1991, Mechanisms of dike propagation in layered rocks and in massive porous sedimentary rocks: Journal of Geophysical Research, v. 96, no. B7, p. 11911–11929.

Barree, R. D., and H. Mukherjee, 1996, Determination of pressure dependent leakoff and its effect on fracture geometry: Society of Petroleum Engineers, SPE 36424, SPE Annual Technical Conference and Exhibition, October 6–9, 1996, 10 p.

Baruch, E., 2009, Seismic sequence stratigraphy of the Barnett Shale, southwestern part of Fort Worth Basin, Texas: Master's thesis, University of Oklahoma, Norman, Oklahoma, 105 p.

Busetti, S., 2009, Fracturing of layered reservoir rocks: Ph.D. dissertation, University of Oklahoma, Norman, Oklahoma, 256 p.

Busetti, S., 2010, Effects of natural fracture reactivation during hydraulic fracturing of the Barnett Shale, Fort Worth Basin, TX: Geological Society of America Abstracts with Programs, v. 42, no. 5, p. 673.

Busetti, S., and Z. Reches, 2007, Formation of network fractures during hydraulic fracturing of the Barnett Shale, a tight gas shale with preexisting fractures (abs.): Eos Transactions of the American Geophysical Union, Fall Meeting Supplement T42C-04, v. 88, no. 52, p. 330.

Busetti, S., W. Jiao, and Z. Reches, Geomechanics of hydraulic fracturing microseismicty: Part 1. Shear, hybrid, and tensile events: AAPG Bulletin, v. 98, p. 2439–2457, doi: 10.1306/05141413123.

Busetti, S., K. Mish, P. Hennings, and Z. Reches, 2012, Damage and plastic deformation of reservoir rocks: Part 2. Propagation of a hydraulic fracture: AAPG Bulletin, v. 96, no. 9, p. 1711–1732.

Byerlee, J. D., and D. Lockner, 1977, Acoustic emission during fluid injection: Proceedings First Conference on Acoustic Emission/microseismic Activity in Geologic Structures and Materials, Pennsylvania State University, Trans Tech Publications, Clausthal, Germany, p. 87–98.

Chitrala, Y., C. Moreno, C. Sondergeld, and C. Rai, 2011, Microseismic and microscopic analysis of laboratory induced hydraulic fractures: Society of Petroleum Engineers, SPE 147321, Canadian Unconventional Resources Conference, November 15–17, 2011, Alberta, Canada, 19 p.

Daniels, J., K. DeLay, G. Waters, L. LeCalvez, J. Lassek, and D. Bentley, 2007, Contacting more of the Barnett Shale through an integration of real-time microseismic monitoring, petrophysics and hydraulic fracturing design: Society of Petroleum Engineers, SPE 110562, SPE ATCE, Anaheim, California, October 12–14, 2007, 12 p.

Dupin, J. M., W. Sassi, and J. Angelier, 1993, Homogeneous stress hypotheses and actual fault slip: a distinct element analysis: Journal of Structural Geology, v. 15, no. 8, p. 1033–1043.

Elebiju, O., 2009, Integrated geophysical investigations of linkages between Precambrian basement and sedimentary structures in the Ucayali Basin, Peru; Fort Worth Basin, Texas; and Osage County, Oklahoma: Ph.D. dissertation, University of Oklahoma, Norman, Oklahoma, 350 p.

Fisher, M. K., C. A. Wright, B. M. Davidson, A. K. Goodwin, E. O. Fielder, W. S. Buckler, and N. P. Steinberger, 2005, Integrating fracture-mapping technologies to improve stimulations in the Barnett Shale: Society of Petroleum Engineers Production and Facilities 77441, p. 85–93.

Gale, J. F. W., and J. Holder, 2008, Natural fractures in the Barnett Shale: Constraints on spatial organization and tensile strength with implications for hydraulic fracture treatment in shale-gas reservoirs, in: Proceedings of the 42nd US Rock Mechanics Symposium. Paper no. ARMA-08-096, 9 p.

Gale, J. F. W., R. M. Reed, and J. Holder, 2007, Natural fractures in the Barnett Shale and their importance for hydraulic fracture treatmetns: AAPG Bulletin, v. 91, no. 4, p. 603–622.

Gephart, J. W., and D. W. Forsyth, 1984, An improved method for determining the regional stress tensor using earthquake focal mechanisms data: an application to the San Fernando earthquake sequence: Journal of Geophysical Research, v. B, v. 89, p. 9305–9320.

Grob, M., and M. van der Baan, 2011, Inferring in situ stress changes by statistical analysis of microseismic event characteristics: The Leading Edge, v. 30, no. 11, p. 1296–1302.

Hardage, B. A., D. L. Carr, D. E. Lancaster, J. L. Simmons, R. Y. Elphick, V. M. Pendleton, and R. A. Johns, 1996, 3-D seismic evidence of the effects of carbonate karst collapse on overlying clastic stratigraphy and reservoir compartmentalization: Geophysics, v. 61, no. 5, p. 1336–1350.

Healy, D., R. R. Jones, and R. E. Holdsworth, 2006, Three-dimensional brittle shear fracturing by tensile crack interaction: Nature, v. 439, no. 7072, p. 64–67.

Hennings, P., P. Allwardt, P. Paul, C. Zahm, R. Reid, Jr., H. Alley, R. Kirschner, B. Lee, and E. Hough, 2012, Relationship between fractures, fault zones, stress, and reservoir productivity in the Suban gas field, Sumatra, Indonesia: AAPG Bulletin, v. 96, no. 4, p. 753–772.

Ishida, T., Q. Chen, M. Yoshiaki, and J. C. Roegiers, 2004, Influence of viscosity on the hydraulic fracturing mechanism: Journal of Energy Resources Technology, v. 126, p. 190–200.

Kassis, S., and C. H. Sondergeld, 2010, Gas shale permeability: effects of roughness, proppant, fracture offset, and confining pressure: Society of Petroleum Engineers, SPE 131376,

International Oil and Gas Conference and Exhibition in China, Beijing, China, June 8–10, 2010, 17 p.

Leclere, H., and O. Fabbri, 2013, A new three-dimensional method of fault reactivation analysis: Journal of Structural Geology, v. 48, p. 153–161.

Loucks, R. G., 1999, Paleocave carbonate reservoirs: origins, burial-depth modifications, spatial complexity, and reservoir implications: AAPG Bulletin, v. 83, p. 1795–1834.

Mayerhofer, M. J., E. P. Lolon, J. E. Youngblood, and J. R. Heinze, 2006, Integration of microseismic fracture mapping results with numerical fracture network production modeling in the Barnett Shale. Society of Petroleum Engineers, SPE 102103, SPE ATCE, San Antonio, September 24–27, 2006, 8 p.

McDonnell, A., R. G. Loucks, and T. Dooley, 2007, Quantifying the origin and geometry of circular sag structures in northern Fort Worth Basin, Texas: paleocave collapse, pull-apart fault systems, or hydrothermal alteration?: AAPG Bulletin, v. 91, no. 9, p. 1295–1318.

Montgomery, S. L., D. M. Jarvie, K. A. Bowker, and R. M. Pollastro, 2005, Mississippian Barnett Shale, Fort Worth Basin, north-central Texas: gas-shale play with multi-trillion cubic foot potential: AAPG Bulletin, v. 89, no. 2, p. 155–175.

Pearson, C., 1981, The relationship between microseismicity and high pore pressures during hydraulic stimulation experiments in low permeability granitic rocks: Journal of Geophysical Research, v. 86, p. 7855–7864.

Pollard, D. D., and P. Segall, 1987, Theoretical displacement and stresses near fractures in rock with application to faults, joints, veins, dikes, and solution surfaces, *in* B. K. Atkinson, ed., Fracture Mechancis of Rock, Academic Press, Inc., p. 277–349.

Pollastro, R. M., D. M. Jarvie, R. J. Hill, and C. W. Adams, 2007, Geologic framework of the Mississippian Barnett Shale, Barnett-Paleozoic total petroleum system, Bend arch-Fort Worth Basin, Texas: AAPG Bulletin, v. 91, no. 4, p. 405–436.

Ramurthy, M., W. Lyons, R. B. Hendrickson, R. D. Barree, and D. P. Magill, 2007, Effects of high pressure dependent leak-off and high process zone stress in coal stimulation treatments: Society of Petroleum Engineers, SPE 107971, SPE Rocky Mountain Oil and Gas Technology Symposium, April 16–18, Denver, Colorado, 8 p.

Reches, Z., 1987, Determination of the tectonic stress tensor from slip analysis along faults that obey the coulomb yield condition: Tectonics, v. 6, no. 6, p. 849–861.

Reches, Z., and D. Lockner, 1994, Nucleation and growth of faults in brittle rocks: Journal of Geophysical Research: Solid Earth, v. 99, no. B9, p. 18159–18173.

Roth, M., and A. Thompson, 2009, Fracture interpretation in the Barnett Shale using macro- and microseismic data: First Break, v. 27, no. 4, p. 83–88.

Roussel, N. P., and M. M. Sharma, 2011, Strategies to minimize frac spacing and stimulate natural fractures in horizontal completions: Society of Petroleum Engineers, SPE 146104, SPE Annual Technical Conference and Exhibition, Denver, Colorado, October 30—November 2, 2011, 17 p.

Roussel, N. P., and M. M. Sharma, 2012, Role of stress reorientation in the success of refracture treatments in tight gas sands: Society of Petroleum Engineers, SPE 134491, SPE Journal, v. 27, no. 4, p. 346–355.

Roy, B., B. Hart, A. Mironova, C. Zhou, and U. Zimmer, 2014, Integrated characterization of hydraulic fracture treatments in the Barnett Shale: the Stocker geophysical experiment, Interpretation, v. 2, no. 2, p. T111–T127, doi:10.1190/INT-2013-0071.1.

Sibson, R. H., 1996, Structural permeability of fluid-driven fault-fracture meshes: Journal of Structural Geology, v. 18, no. 8, p. 1031–1042.

Sil, S., B. Bankhead, C. Zhou, and A. Sena, 2012, Analysis of B value from Barnett Shale microseismic data: 74th EAGE Conference & Exhibition incorporating SPE EUROPEC 2012, Copenhagen, Denmark, June 4–7, 2012, p. 1225–1229.

Simon, Y., 2005, Stress and fracture characterization in a shale reservoir, North Texas, using correlation between new seismic attributes and well data: Master's thesis, University of Oklahoma, Norman, Oklahoma, 84 p.

Singh, P., 2008, Lithofacies and sequence stratigraphic framework of the Barnett Shale, Northeast Texas: Ph.D. dissertation, University of Oklahoma, Norman, Oklahoma, 181 p.

Sneddon, I. N., 1946, The distribution of stress in the neighborhood of a crack in an elastic solid: Proceedings of the Royal Society of London, v. A187, no. 1009, p. 229–260.

Vavryčuk, V., 2001, Inversion for parameters of tensile earthquakes: Journal of Geophysical Research, v. 106, no. B8, p. 16,339–16,355.

Vavryčuk, V., 2011, Tensile earthquakes: theory, modeling, and inversion: Journal of Geophysical Research, v. 116, no. B12, 320, p. 1–14.

Vermylen, J., and M. D. Zoback, 2011, Hydraulic fracturing, microseismic magnitudes, and stress evolution in the Barnett Shale, Texas, USA: Society of Petroleum Engineers, SPE 140507, SPE Hydraulic Fracturing Technology Conference and Exhibition, January 24–26, 2011, The Woodlands, Texas, 15 p.

Walper, J. L., 1982, Plate tectonic evolution of the Fort Worth basin, *in* C. A. Martin, ed., Petroleum Geology of the Fort Worth basin and Bend arch area, Dallas Geological Society, p. 237–351.

Zoback, M. D., 2007, Reservoir Geomechanics: New York, Cambridge University Press, 449 p.

Zoback, M. D., A. Kohli, I. Das, and M. McClure, 2012, The importance of slow slip on faults during hydraulic fracturing stimulation of shale gas reservoirs: Society of Petroleum Engineers, SPE 155476, SPE Americas Unconventional Resources Conference, June 5–7 2012, Pittsburgh, Pennsylvania, 9 p.